Quantum phase transition in a quantum Rabi square with next-nearest-neighbor hopping

Yilun Xu,[1,2] Feng-Xiao Sun,[1,3,*] Qiongyi He,[1,3] Han Pu,[4] and Wei Zhang[2,5]

[1]*State Key Laboratory for Mesoscopic Physics, School of Physics, Frontiers Science Center for Nano-optoelectronics, Peking University, Beijing 100871, China*

[2]*Beijing Academy of Quantum Information Sciences, Beijing 100193, China*

[3]*Collaborative Innovation Center of Extreme Optics, Shanxi University, Taiyuan, Shanxi 030006, China*

[4]*Department of Physics and Astronomy, Rice University, Houston, Texas 77251-1892, USA*

[5]*Department of Physics and Key Laboratory of Quantum State Construction and Manipulation (Ministry of Education), Renmin University of China, Beijing 100872, China*

(Received 18 February 2024; accepted 3 July 2024; published 1 August 2024)

We propose a quantum Rabi square model where both the nearest-neighbor and the next-nearest-neighbor photon hopping are allowed among four quantum Rabi systems located at the vertices of a square. By tuning the next-nearest hopping strength, we realize a first-order phase transition between the antiferromagnetic superradiant phase and the frustrated superradiant phase, as well as a second-order phase transition between the normal and the superradiant phases. To understand the emergence of such phases, we show analytically that the effect induced by next-nearest hopping is equivalent to that of an artificial gauge phase. Our findings suggest that the next-nearest-neighbor hopping can serve as an alternative for the gauge phase to realize quantum control in applications of quantum simulation and quantum materials and that our model represents a basic building block for the frustrated J_1-J_2 quantum spin model on square lattices.

DOI: 10.1103/PhysRevA.110.023702

I. INTRODUCTION

The study of quantum phase transitions (QPTs) in systems of light-matter interaction has remained at the frontier of quantum optics and atomic physics for more than a century. A prototypical model supporting the QPT is the Dicke model [1–4], where a superradiant phase transition is induced by the strong atom-light interaction and the thermodynamic limit can be satisfied if the atom number $N \to \infty$. Later, the QPT was revealed in the quantum Rabi model (QRM) and the Jaynes-Cummings model [5,6], where a single-mode cavity field and a two-level atom are coupled. With the fast development of experimental techniques, significant progress has been achieved in realizing strong light-matter coupling and controlling related parameters, making it possible to demonstrate the QPT in well-controlled manners [7–19]. There has been much interest in the investigation of exotic quantum phases in models such as the QRM [5,20–25], the Jaynes-Cummings lattice model [6,26], the Tavis-Cummings model [27], the Dicke model [28–34], and so on [35–37].

Among them, QPTs in coupled few-cavity systems, such as in a Rabi dimer (chain) [23], a Jaynes-Cummings dimer (chain) [6], a quantum Rabi trimer (ring) [20,21], and a Dicke trimer [31], have been proposed to simulate and investigate emergent phenomena in strongly correlated systems. Various intriguing phenomena traditionally explored in condensed-matter physics can be observed in such light-matter coupled systems. In particular, it has been suggested that a one-dimensional coupled array of cavity systems with an artificial gauge field can be mapped to a chiral magnetic model consisting of various kinds of magnetic couplings and present rich phase diagrams of magnetic orders [20,21]. In such examples, the nontrivial phase of the photon hopping amplitude results from the synthetic gauge field, which breaks the time-reversal symmetry and plays a crucial role in determining the quantum phases of the system. However, the realization and manipulation of the synthetic gauge field are usually technically challenging tasks. Considering the long-lasting interest in investigating quantum magnetic phases, it is then desirable to seek alternative approaches to realize a similar effect without the need of a synthetic gauge field.

One promising route to induce exotic phases is through hopping of longer range than nearest neighbors. To this end, the atom-photon platform offers a unique advantage in realizing and manipulating such long-range coupling, which is usually very weak and does not have much room to vary in solids. Long-range coupling has been realized in photonic systems [38–40], cold atoms [41,42], trapped ions [43], and superconducting qubits [44]. This experimental progress suggests the use of long-range coupling as a useful tool for realizing and studying quantum phases. As we will show here, as a potential substitute for the synthetic gauge field, the quantum Rabi lattices with beyond-nearest-neighbor hopping provides new possibilities to manipulate various quantum phases.

In this paper we study a quantum Rabi square (QRS) model constructed of four QRMs of an interacting two-level atom and a cavity photon, residing on the vertices of a square, as schematically depicted in Fig. 1. The QRMs are coupled by both the nearest-neighbor and the next-nearest-neighbor photon hopping, with respective hopping amplitudes J_1

*Contact author: sunfengxiao@pku.edu.cn

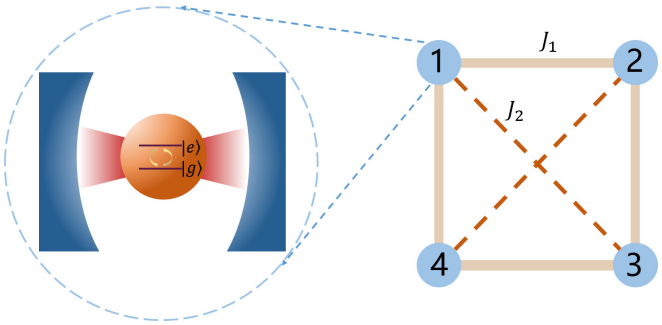

FIG. 1. Schematic diagram of the QRS model. Four individual QRMs with identical parameters are located in the vertices of a square lattice, respectively, with the nearest hopping J_1 and the next-nearest hopping J_2 included in the lattice.

and J_2. We consider both hopping parameters to be of real values and hence there is no artificial gauge field present. From a different perspective, our model can also be regarded as a building block for the J_1-J_2 spin Heisenberg model [45–47], which has been extensively studied in quantum magnetism and hence can shed light on the implementation and investigation of interacting spin models.

By treating the cavity photon via a mean-field approximation, we obtain an analytic solution of the ground state and map out the phase diagram by tuning the atom-light coupling and the relative hopping strength of J_2/J_1. When the atom-light coupling is weak, all QRMs are in the normal phase (NP) with zero expectation of a cavity photon. By increasing the coupling strength across the critical point, the system will go through a second-order phase transition to enter a superradiant phase (SRP) along with the spontaneous breaking of the Z_2 symmetry of photons and geometric C_4 symmetry of the square. The SRP can be further divided into two branches distinguished by the symmetry of the ground state when tuning the next-nearest-neighbor hopping. The two different branches of the SRP can be mapped to (anti)ferromagnetic and frustrated phases of quantum magnetic models, which are also observed in the quantum Rabi ring (QRR) model involving the artificial gauge phase [20,21]. Finally, we derive an analytic correspondence between the next-nearest-neighbor hopping and gauge field for this model. Our work suggests the usage of long-range coupling as a versatile tool in the simulation and study of QPTs.

II. QUANTUM RABI SQUARE MODEL

We consider a QRS model constructed of four identical QRMs sitting on the vertices of a square, as shown in Fig. 1. Each QRM is coupled with its two nearest neighbors with a photon hopping amplitude J_1 (edges of the square) and with the opposite node with hopping amplitude J_2 (diagonals). The system Hamiltonian reads

$$H = \sum_{i=1}^{4} H_{R,i} + H_{\rm hop} + H_{\rm next},$$

$$H_{R,i} = \omega a_i^\dagger a_i + \frac{\Omega}{2}\sigma_i^z + \lambda(a_i^\dagger + a_i)\sigma_i^x,$$

$$H_{\rm hop} = \sum_{i=1}^{4} J_1 a_i a_{i+1}^\dagger + \text{H.c.},$$

$$H_{\rm next} = J_2(a_1 a_3^\dagger + a_2 a_4^\dagger + \text{H.c.}). \quad (1)$$

In the Hamiltonian of the QRM on the ith site $H_{R,i}$, a_i and $a_i^\dagger$ are the field operators for the optical field and σ_i^z stands for the Pauli spin operator in the z direction for the two-level atom. The four QRMs have the same photon frequency ω, the energy gap of the two-level atom Ω, and the cavity-atom coupling strength λ. The general scenario of nonidentical nodes can be investigated analogously. The nearest-neighbor and next-nearest-neighbor hopping of photons are represented by $H_{\rm hop}$ and $H_{\rm next}$, respectively. Notice that here we consider only real values for both J_1 and J_2. Thus, the system does not possess any gauge field, which is the main focus of the previously studied quantum Rabi ring model [20,21].

When all the couplings between the four sites are zero, the system consists of four identical and isolated QRMs, which can host a QPT between the NP and SRP [5], in the so-called classical oscillator limit, i.e., $\Omega/\omega \to \infty$. This is because the macroscopic photonic occupation of the cavity mode is proportional to Ω/ω. By turning on a finite nearest-neighbor hopping J_1, the system can present a richer phase diagram with multiple superradiant phases showing magnetic and chiral signatures [21]. A recent theoretical study involved the next-nearest-neighbor coupling J_2 for a one-dimensional Dicke lattice model [34]. However, the effect of such long-range hopping on the SRPs is still an open question.

Before showing our main results in detail, we briefly analyze the symmetry of the QRS model. The parity symmetry of the total excitation number is preserved in the QRS, which is isomorphic to the Z_2 symmetry. Defining the parity operator as $\hat{P} = \exp(i\pi \sum_{i=1}^{4} \hat{N}_i)$, where $\hat{N}_i \equiv a_i^\dagger a_i + \sigma_i^+\sigma_i^-$ represents the excitation number of the ith cavity, the commutation relation $[H, \hat{P}] = 0$ can be easily verified. The two eigenvalues of the parity operator are ± 1, denoting the vectors in subspace with even or odd total excitations, respectively. Furthermore, the cyclic symmetry is also present in this Hamiltonian. This means that the system remains unchanged by rotating the four sites as $1234 \to 2341 \to 3412 \to 4123$, which composes the element of the C_4 group. Thus, the Hamiltonian H follows a total $Z_2 \times C_4$ symmetry.

III. NORMAL PHASE

With the aid of the Schrieffer-Wolff transformation, the original Hamiltonian (1) can be simplified. The idea of the Schrieffer-Wolff transformation is to rotate the system into another representation by a well-designed unitary operator $U = e^S$, where S is an anti-Hermitian operator and the coupling between the spin-up and spin-down subspaces can be effectively eliminated by the term $[H, S]$. The transformation matrix can be expressed as $U = \Pi_n U_n$, where $U_n = \exp[-i\frac{g}{\sqrt{\eta}}\sigma_n^y(a_n^\dagger + a_n)]$. Here the two key dimensionless parameters are defined as

$$g \equiv \lambda/\sqrt{\Omega\omega}, \quad \eta \equiv \Omega/\omega,$$

representing the normalized atom-cavity coupling strength and the ratio of the atomic and the photon frequencies, respectively. The normalized coupling strength is kept finite in our discussion, and the hopping strengths among the sites are much lower than the frequencies of the optical modes. In summary, the parameters of the model are assumed to satisfy $\Omega \gg \lambda \gg \omega \gg J_1, J_2$.

Taking this condition into account, the effective Hamiltonian after the Schrieffer-Wolff transformation can be calculated through $H^{\text{eff}} = e^{-S} H e^{S}$, resulting in

$$\begin{aligned} H^{\text{eff}} &= \sum_{i=1}^{4} H_{R,i}^{\text{eff}} + H_{\text{hop}} + H_{\text{next}} + O(\omega\eta^{-1}), \\ H_{R,i}^{\text{eff}} &= \omega a_i^\dagger a_i + \frac{\Omega}{2}\sigma_i^z + \omega g^2 \sigma_i^z (a_i + a_i^\dagger)^2. \end{aligned} \tag{2}$$

After projecting the effective Hamiltonian into the four-fold spin-down subspace, i.e., $H_{\downarrow}^{\text{eff}} \equiv \text{tr}[(|\downarrow\rangle\langle\downarrow|)^{\otimes 4} H^{\text{eff}}]$, the Hamiltonian will take the form

$$\begin{aligned} H_{\downarrow}^{\text{eff}} &= \sum_{i=1}^{4} (\omega - 2\omega g^2) a_i^\dagger a_i - \omega g^2 \left(a_i^2 + a_i^{\dagger 2}\right) \\ &\quad + \sum_{i,j=1}^{4} a_i^\dagger M_{ij} a_j + E_0, \\ E_0 &= 4\left(-\frac{\Omega}{2} - \omega g^2 + \frac{\omega^2 g^2}{\Omega}\right), \\ M &= \begin{pmatrix} 0 & J_1 & J_2 & J_1 \\ J_1 & 0 & J_1 & J_2 \\ J_2 & J_1 & 0 & J_1 \\ J_1 & J_2 & J_1 & 0 \end{pmatrix}. \end{aligned} \tag{3}$$

The term $\sum_{i,j=1}^{4} a_i^\dagger M_{ij} a_j$ originates from the nearest- and next-nearest-neighbor hopping interaction $H_{\text{hop}} + H_{\text{next}}$.

Since the translation invariance is preserved in this system, the Bloch theorem can be applied. To this end, we transform the creation and annihilation operators into momentum space as $a_n^\dagger = (1/\sqrt{N}) \sum_{n=1}^{N} e^{inq} a_q^\dagger$, where $q = 2\pi l/N$ is the system momentum, with $l = 0, 1, \ldots, N-1$ and $N = 4$ for our QRS model. By means of this transformation, the Hamiltonian in momentum space can be expressed as

$$H_{\downarrow}^{\text{eff}} = \sum_{q} [\omega_q a_q^\dagger a_q - \omega g^2 (a_q a_{-q} + a_q^\dagger a_{-q}^\dagger)] + E_0, \tag{4}$$

where $\omega_q = \omega - 2\omega g^2 + J_2 \cos(2q) + 2J_1 \cos(q)$. Then, using the two-mode squeezing transformation, i.e., the Bogoliubov transformation $S_q = \exp[\lambda_q (a_q^\dagger a_{-q}^\dagger - a_q a_{-q})]$, with $\lambda_q = \frac{1}{8} \ln \frac{\omega_q + \omega_{-q} + 4\omega g^2}{\omega_q + \omega_{-q} - 4\omega g^2}$, we can obtain the ground-state energy E_g and the excitation energy ε_q,

$$\begin{aligned} E_g &= E_0 + \frac{1}{2} \sum_{q} (\varepsilon_q - \omega_q), \\ \varepsilon_q &= \frac{1}{2} [\sqrt{(\omega_q + \omega_{-q})^2 - 16\omega^2 g^4} + \omega_q - \omega_{-q}], \end{aligned} \tag{5}$$

and write the effective Hamiltonian as $H_{\downarrow}^{\text{eff}} = \sum_q \varepsilon_q a_q^\dagger a_q + E_g$. The critical points will be reached when the excited energy ε_q vanishes, giving

$$4g_c^2(q) = 1 + \frac{J_2}{\omega} \cos(2q) + \frac{2J_1}{\omega} \cos(q). \tag{6}$$

It is straightforward to verify that $g_c(\pi/2) = g_c(3\pi/2)$ and $g_c(\pi) < g_c(0)$ when $J_1 > 0$. Thus, we only need to focus on the two branches of the SRP denoted by $q = \pi$ and $q = \pi/2$ $(3\pi/2)$ for $J_1 > 0$. For the case of $J_1 < 0$, a similar analysis can be carried out and will be briefly discussed later.

IV. SUPERRADIANT PHASE

When the dimensionless coupling strength g exceeds the critical point g_c, the first-excited energy derived in the preceding section [i.e., Eq. (5)] will be revised and the superradiant phase transition occurs. By treating the optical mode via a mean-field approach, the annihilation operator can be rewritten as $a_n \to a_n + \alpha_n$, where the mean value of the optical field amplitude is complex and defined as $\alpha_n = A_n + iB_n$. Then the Hamiltonian becomes

$$\begin{aligned} H &= \sum_{n} \Big(\omega a_n^\dagger a_n + \frac{\Omega_n}{2} \tau_n^z + \lambda_n (a_n + a_n^\dagger) \tau_n^x \\ &\quad + J_1 a_n^\dagger (a_{n+1} + a_{n-1}) + J_2 a_n^\dagger a_{n+2} \Big) + V + E_0, \\ E_0 &= \sum_{n} |\alpha_n|^2 + J_1 \sum_{n} \alpha_n^* (\alpha_{n+1} + \alpha_{n-1}) + J_2 \sum_{n} \alpha_n^* \alpha_{n+2}, \\ V &= \sum_{n} \{ \omega(\alpha_n a_n^\dagger + \alpha_n^* a_n) + \lambda \sin(2\gamma_n) \tau_n^z (a_n^\dagger + a_n) \\ &\quad + J_1 [a_n^\dagger (\alpha_{n+1} + \alpha_{n-1}) + \text{H.c.}] + J_2 (a_n^\dagger \alpha_{n+2} + \text{H.c.}) \}, \end{aligned} \tag{7}$$

where the transformed Pauli Z operator $\tau_n^z = (\Omega\sigma_n^z + 4A_n\lambda\sigma_n^x)/\Omega_n$ and $\Omega_n = \sqrt{\Omega^2 + 16\lambda^2 A_n^2}$. Then the eigenvectors of τ_n^z can be obtained as

$$\begin{aligned} |+\rangle &= \cos(\gamma_n) |\uparrow\rangle + \sin(\gamma_n) |\downarrow\rangle, \\ |-\rangle &= -\sin(\gamma_n) |\uparrow\rangle + \cos(\gamma_n) |\downarrow\rangle, \end{aligned} \tag{8}$$

where $\tan(2\gamma_n) = 4\lambda A_n/\Omega$.

Typically, the local minimum can be determined by demanding $V = 0$, which will give us the concrete value for the optical displacement $\{\alpha_n\}$ in Appendix A. Then the Hamiltonian retains only two parts in the form

$$\begin{aligned} H &= \sum_{n} \Big(\omega a_n^\dagger a_n + \frac{\Omega_n}{2} \tau_n^z + \lambda_n (a_n + a_n^\dagger) \tau_n^x \\ &\quad + J_1 a_n^\dagger (a_{n+1} + a_{n-1}) + J_2 a_n^\dagger a_{n+2} \Big) + E_0. \end{aligned} \tag{9}$$

Notice that the mean-field Hamiltonian (9) acquires a form similar to the original Hamiltonian (1). Thus, we can employ the same approach to obtain the ground-state energy, which

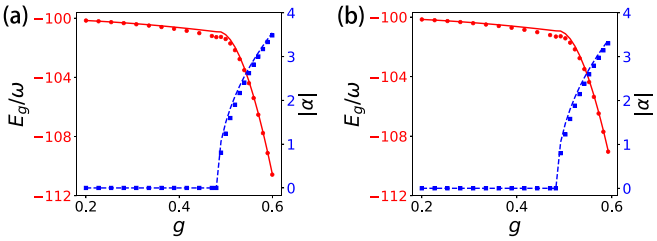

FIG. 2. Ground-state energy E_g (red solid line with circles) and order parameter $|\alpha|$ (blue dashed line with squares) with (a) $J_2 = 0.02$ and (b) $J_2 = 0.07$. The numerical results (circles and squares) agree well with the analytical results (red solid and blue dashed lines). We set the fixed parameters $\Omega = 50$, $J_1 = 0.05$, and $\omega = 1$ as the unit of energy in all the figures of this paper.

reads

$$E_g = \sum_n \Big\{ \omega\big(A_n^2 + B_n^2\big) + 2J_1[(A_nA_{n+1} + B_nB_{n+1})] + J_2(A_nA_{n+2} + B_nB_{n+2}) - \frac{1}{2}\Omega_n \Big\} + \sum_n \left(-\omega g_n^2 + \frac{\omega^2 g_n^2}{\Omega_n}\right) + \frac{1}{2}\sum_q (\varepsilon'_q - \omega'_q). \quad (10)$$

Here $g_n = \lambda_n/\sqrt{\omega\Omega_n}$ and $\lambda_n = \lambda\Omega/\Omega_n$. By minimizing the first two lines of (10), which serve as the main contribution to the ground-state energy, we can also get the same solutions for A_n and B_n as the ones in Appendix A. In the QRS, g_n and Ω_n are independent of the site index n, so we denote all the g_n and Ω_n by g' and Ω' in the following. The ground-state energy for all three branches is summarized as

$$E_g = -\left(\frac{\lambda^2}{g_c^2(q_0)\omega} + \frac{\Omega^2}{\lambda^2} g_c^2(q_0)\omega\right) + 4\left(-\omega g'^2 + \frac{\omega^2 g'^2}{\Omega'}\right) + \frac{1}{2}\sum_q (\varepsilon'_q - \omega'_q). \quad (11)$$

Here $\varepsilon'_q = \frac{1}{2}[\sqrt{(\omega'_q + \omega'_{-q})^2 - 16\omega^2 g'^4} + \omega'_q - \omega'_{-q}]$, with $\omega'_q = \omega - 2\omega g'^2 + J_2\cos(2q) + 2J_1\cos(q)$ the excitation energy of the SRP, which acquires a similar form as in the NP with g replaced by g'. Note that g' can be expressed in terms of g and g_c as $g' = g_c^3(q_0)/g^2$, if we combine the definition $g' = \lambda'/\sqrt{\omega\Omega'}$ with the identities

$$\Omega' = \sqrt{\Omega^2 + 16\lambda^2 A^2},$$
$$A^2 = \frac{1}{16\lambda^2}\left(\frac{16\lambda^4}{\big[4\omega g_c^2(q_0)\big]^2} - \Omega^2\right),$$
$$\lambda' = \lambda_n = \frac{\lambda\Omega}{\Omega'}. \quad (12)$$

The ground-state energy E_g and the order parameter $|\alpha|$ are depicted in Fig. 2, where J_2 is set equal to 0.02 and 0.07 in Figs. 2(a) and 2(b), respectively. In both cases, numerical simulations (red circles and blue squares) are obtained for comparison by diagonalizing the displaced Hamiltonian $D(\vec{\alpha})HD^\dagger(\vec{\alpha})$, where H is the original Hamiltonian (1), $\vec{\alpha} \equiv [\alpha_1, \alpha_2, \alpha_3, \alpha_4]^T$, and $D(\vec{\alpha}) \equiv \Pi_n D(\alpha_n) = \Pi_n \exp(\alpha_n^* a_n - \alpha_n a_n^\dagger)$ stands for the total displacement

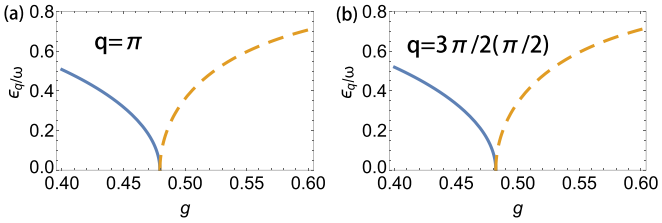

FIG. 3. Excited energy scaling around the critical point with (a) $J_2 = 0.02$ and (b) $J_2 = 0.07$. Here the solid lines correspond to the normal phase and the dashed lines represent the superradiant phase, with the branch of (a) $q = \pi$ and (b) $q = \pi/2$ $(3\pi/2)$ dominating.

operator. The truncated dimension of all four bosonic modes is $N_c = 5$ to guarantee convergence. These numerical results agree well with the analytical solutions (red solid and blue dashed lines). Additionally, the first-order derivative of the order parameter and the second-order derivative of the ground-state energy are discontinuous around the critical points, indicating a second-order QPT. The accuracy of the analytical mean-field ground state is analyzed in Appendix B by comparing with numerical results obtained by exact diagonalization.

To characterize the QPT between the NP and the SRP, next we analyze the scaling behavior of the excitation energy near the critical point $g = g_c(q_0)$. It is easy to verify that $\omega_q = \omega_{-q}$ for the NP and $\omega'_q = \omega'_{-q}$ for all possible SRP branches with $q = \{0, \pi/2, \pi, 3\pi/2\}$. Thus, the excited energy in the NP and SRP can be reduced to $\varepsilon_q = \sqrt{\omega_q^2 - 4\omega^2 g^4}$ and $\varepsilon'_q = \sqrt{\omega_q'^2 - 4\omega^2 g'^4}$, respectively. Taking the NP as an example, we can expand the two terms in the square root up to linear order as $\omega_q^2(g) \sim \omega_q^2(g_c) + k_1(g - g_c)$ and $4\omega^2 g^4 \sim 4\omega^2 g_c^4 + k_2(g - g_c)$, where $k_1 < 0$ and $k_2 > 0$. The combination of them thus gives a nonzero linear coefficient $(k_1 - k_2)$ in the expansion of ε_q. The same analysis can also be applied to the SRP and lead to a linear term as well. With that, the excited energy around $g \to g_c$ scales as $\varepsilon_q, \varepsilon'_q \propto |g - g_c|^{1/2}$. The behaviors of the excited energy around the critical point are demonstrated in Fig. 3, where the SRP branch is $q = \pi$ with $J_2 = 0.02$ in Fig. 3(a) and $q = \pi/2\,(3\pi/2)$ with $J_2 = 0.07$ in Fig. 3(b). In both cases, a typical $1/2$ scaling rule is clearly observed.

V. PHASE DIAGRAM AND CONNECTION TO QUANTUM MAGNETISM

To analyze the phase diagram of the different SRP branches, we follow the discussion of Ref. [21] to consider the real part A_n and imaginary part B_n of the mean-field amplitude of the optical mode as two different directions of the spin operator. As shown in Appendix C, the effective low-energy Hamiltonian (3) can be mapped into a spin J_1-J_2 model. With that, the SRP branches with different choices of q can be characterized by the structure of four local spins and linked to different phases of quantum magnetism. The optical displacements also match well with the spin arrangements. Specifically, in the $q = 0$ branch of the SRP, the spins are mostly aligned, being analogous to the ferromagnetic

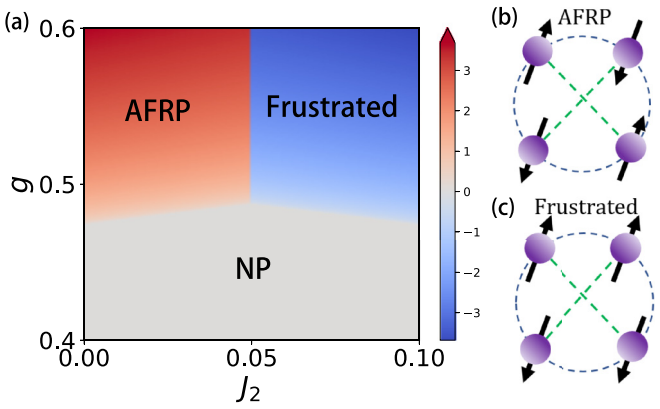

FIG. 4. (a) Phase diagram with a fixed value of the nearest coupling strength $J_1 = 0.05$. The bottom (gray) region corresponds to the NP, the upper left (red) region to the AFRP, and the upper right (blue) region to the frustrated SRP. The spin directions are displayed when the system is located in the (b) AFRP and (c) frustrated phase, respectively.

superradiant phase (FRP). In the $q = \pi$ branch, neighboring spins are antialigned to demonstrate features of the antiferromagnetic superradiant phase (AFRP). The $q = \pi/2$ $(3\pi/2)$ branch presents a spin structure with competing aligned and antialigned tendencies and thus can be referred to as a frustrated magnetic phase.

In Fig. 4(a) we depict the phase diagram against the next-nearest-neighbor hopping J_2 and the atom-cavity coupling g, for a fixed nearest-neighbor hopping $J_1 = 0.05$. Three phases can be clearly found in this phase diagram, with the background color denoting $\alpha_n\alpha_{n+2}/|\alpha|$. Thus the positive and negative values represent the AFRP and frustrated SRP phases, respectively. For small g, the system is in the NP region, as expected. As g goes beyond the critical value, the system crosses a second-order QPT to become a SRP. When $J_2 < J_1$, the $q = \pi$ branch is stabilized and the spins are organized antiferromagnetically to form an AFRP, as shown in Fig. 4(b). When $J_2 > J_1$, the $q = \pi/2$ $(3\pi/2)$ branch is favored to present frustrated spin structures as illustrated in Fig. 4(c). The physical mechanism of the spin frustration can be understood as follows. When the next-nearest-neighbor coupling J_2 is large enough, the spins connected by diagonal lines tend to be antialigned. Meanwhile, the nearest-neighbor hopping also favors antialigned spins connected by edges. These constraints clearly lead to a frustrated spin configuration with both Z_2 and C_4 symmetries broken. As a four-site lattice, the emergency of this frustrated phase also serves as strong evidence for the true frustration effect as the number of sites increases towards infinity. The two SRP branches are separated by a first-order QPT with an abrupt change of spin arrangement. If the nearest-neighbor hopping J_1 is negative, the phase diagram has the form in Fig. 4(a), with the AFRP region being replaced by the FRP since the $q = 0$ branch is more favorable.

VI. CONNECTION TO THE QRR MODEL WITH ARTIFICIAL GAUGE FIELD

Next we discuss the connection between the QRS model with next-nearest-neighbor coupling and the QRR model with an artificial gauge field. The latter is obtained from our model by taking $J_2 = 0$ but making $J_1 \to J_1^0 e^{i\theta}$ complex. It has been shown that the QRR with an artificial gauge field can be mapped to a magnetic system of the coupled Lipkin-Meshkov-Glick model [21] and has potential application in the simulation and study of magnetic orders. In the following, we show analytically that by using the next-nearest-neighbor coupling instead of the gauge phase, both the energy spectrum and eigenfunctions can be exactly recovered.

A. Excitation energy

We first focus on the excitation energy and derive a mapping between the QRS and QRR models. To distinguish these two models, a superscript 0 is used to denote the physical quantities already introduced for the QRS model in the QRR model, without further specification. The excitation energies for the NP (ε_q^0) and SRP ($\varepsilon_q'^0$) in the QRR model are given as

$$\varepsilon_q^0 = \frac{1}{2}\Big[\sqrt{\left(\omega_q^0 + \omega_{-q}^0\right)^2 - 16\omega^2 g^4} + \omega_q^0 - \omega_{-q}^0\Big],$$
$$\varepsilon_q'^0 = \frac{1}{2}\Big[\sqrt{\left(\omega_q'^0 + \omega_{-q}'^0\right)^2 - 16\omega^2 (g'^0)^4} + \omega_q'^0 - \omega_{-q}'^0\Big], \quad (13)$$

where $\omega_q^0 = \omega - 2\omega g^2 + 2J_1^0\cos(q-\theta)$, $\omega_q'^0 = \omega - 2\omega(g'^0)^2 + 2J_1^0\cos(q-\theta)$, and the renormalized coupling strength can be expressed by the critical points in the QRR model as $g'^0 = (g_c^0)^3 q_0/g^2$. Thus, the critical points for different q read

$$4\left(g_c^0\right)^2 q = \frac{1 + \frac{4J_1^0}{\omega}\cos(q)\cos(\theta) + \frac{4(J_1^0)^2}{\omega^2}\cos(q-\theta)\cos(q+\theta)}{1 + \frac{2J_1^0}{\omega}\cos(q)\cos(\theta)}. \quad (14)$$

The relation between the QRS and QRR models can be established by demanding that the excitation energies therein be equal. Because the critical points are also derived by setting the excitation energy to zero, the critical points and resulting phase diagram can be naturally reproduced.

1. Correspondence to the AFRP

By setting $q = \pi$, we reach the following conditions in the NP and SRP, respectively:

$$\varepsilon_\pi^0(\theta) = \varepsilon_\pi(J_2),$$
$$\varepsilon_\pi'^0(\theta) = \varepsilon_\pi'(J_2). \quad (15)$$

Therefore, we can get the constraints for θ and J_2, leading to

$$J_2 = 2\big[J_1 - J_1^0\cos(\theta)\big]. \quad (16)$$

This relation establishes an exact connection between the next-nearest-neighbor hopping J_2 and gauge phase θ.

2. Correspondence to the frustrated SRP

Since the cases of $q = 3\pi/2$ and $\pi/2$ are equivalent, in the following we set $q = 3\pi/2$ for simplicity. The matching

conditions for the NP and SRP are

$$\varepsilon^0_{3\pi/2}(\theta) = \varepsilon_{3\pi/2}(J_2),$$
$$\varepsilon'^0_{3\pi/2}(\theta) = \varepsilon'_{3\pi/2}(J_2). \tag{17}$$

In addition, we can obtain the condition of the parameters for the two phases as

$$J_2 = 1 - 2g^2 - \sqrt{\left[\sqrt{1-4g^2} - 2J_1^0\sin(\theta)\right]^2 + 4g^4},$$
$$J_2 = 1 - 2g'^2 - \sqrt{\left[\sqrt{1-4g'^2} - 2J_1^0\sin(\theta)\right]^2 + 4g'^4}. \tag{18}$$

Notice that here the connection between J_2 and θ is of different form for the NP and SRP, which join at the critical point to form a continuous function of the dimensionless atom-cavity coupling strength g. The value of J_2 at the critical point is obtained as $J_2(g = g_c) = 4(J_1^0)^2\sin^2(\theta)$, by inserting $g = g_c(3\pi/2) = \frac{1}{2}\sqrt{1-4(J_1^0)^2\sin^2(\theta)}$.

3. Boundary for the first-order phase transition

In QRR model with $J_2 = 0$, the boundary between the $q = \pi$ and $q = \pi/2$ ($3\pi/2$) phases is given by the intersection of the corresponding critical curves, and the coordinate for the intersection θ_c can be determined by the equation

$$1 - 2J_1^0\cos(\theta_c) = 1 - 4\left(J_1^0\right)^2\sin^2(\theta_c). \tag{19}$$

In the QRS model, the critical point for the first-order phase transition is given by $J_{2c} = J_1$. Combining Eqs. (16) and (18), it can be derived that

$$J_1 = J_{2c} = 2\left[J_1 - J_1^0\cos(\theta_c)\right],$$
$$J_1 = J_{2c}(g = g_c) = d34\left(J_1^0\right)^2\sin^2(\theta_c). \tag{20}$$

The value of the nearest hopping rate J_1 hence can be determined as $J_1 = 2J_1^0\cos(\theta_c)$ by the first condition and $J_1 = 4(J_1^0)^2\sin^2(\theta_c)$ by the second condition. The two solutions are identical according to Eq. (19).

4. Case of negative J_1 and the FRP

If we set the nearest hopping strength $J_1 < 0$, the FRP region can also be simulated in our model with a similar analysis. In such a case, the AFRP vanishes, while the first-order phase transition between the FRP and the frustrated SRP can also be observed. In addition, all of the above discussion is still valid after replacing J_1 and θ by $-J_1$ and $\pi - \theta$, respectively.

B. Order parameter

We can also establish a mapping between the QRS and QRR models by requiring the same order parameter A^2, i.e., displacement for optical modes. In both models, A^2 is written

$$A^2 = \frac{1}{16\lambda^2}\left(\frac{16\lambda^4}{\left[4\omega g_c^2(q_0)\right]^2} - \Omega^2\right). \tag{21}$$

Obviously, the same critical point is obtained in this mapping. According to Eq. (14), the conditions for the AFRP and the frustrated SRP are achieved as

$$J_2 = 2\left[J_1 - J_1^0\cos(\theta)\right],$$
$$J_2 = 4\left(J_1^0\right)^2\sin^2(\theta), \tag{22}$$

respectively. In order to acquire the same triple point, we also require $J_{2c} = 2[J_1 - J_1^0\cos(\theta_c)] = J_1$, giving $J_1 = 2J_1^0\cos(\theta_c)$, or equivalently $J_{2c} = 4(J_1^0)^2\sin^2(\theta_c) = J_1$. Similar mapping for the SRP can be reached by setting the negative nearest hopping rate $J_1 < 0$. We emphasize that while the relation between J_2 and θ in the AFRP is the same as the one derived from excitation energy, for the frustrated SRP the condition in Eq. (22) is different from that in Eq. (18).

To summarize, the previously studied QRR model with nearest-neighbor hopping strength J_1^0 and gauge phase θ can be equivalently investigated by using our QRS model without any gauge phases. In order to obtain the same excitation energy, J_2 is determined by Eqs. (16) and (18). When it comes to the order parameter, the matching conditions give Eq. (22). These two considerations give the same requirement of $J_1 = 2J_1^0\cos(\theta_c)$ to reach the same triple point and phase diagram. Here θ_c is obtained through $2J_1^0\cos(\theta_c) = 4(J_1^0)^2\sin^2(\theta_c)$. In this aspect, the next-nearest-neighbor hopping can play the same role as the artificial gauge phase. Considering the fact that an experimental realization of the synthetic gauge field usually requires a fine-tuning of the hopping parameter via some complex schemes, e.g., by applying Floquet engineering [20,48], and may introduce side effects such as heating and noises, our work provides another route to implement and explore exotic phases in certain experimentally friendly platforms [19,49], which involve only real hopping amplitudes.

VII. SUMMARY

In this paper we proposed a quantum Rabi square model where the effect of the next-nearest neighbor hopping strength was mainly investigated. We obtained the analytical ground-state energy and the critical points for both the first- and the second-order phase transitions. We saw that the equivalent spin arrangement of the optical modes will go through a sudden change when the next-nearest hopping strength exceeds the nearest hopping rate. Comparing with the previous work on the QRR model [21], we found that our model provides an alternative approach to realize the global gauge phase by means of the next-nearest hopping strength. The one-to-one corresponding relations between θ in the QRR and J_2 in the QRS were also obtained from the excited energy and order parameter, respectively. With these results, it could be concluded that the gauge phase plays the same role as an appropriate additional system parameter, such as the next-nearest hopping rate J_2 in our QRS model, which offers a crucial explanation on how the gauge phase induces exotic quantum phases. Those extra degrees of freedom will lead to staggered critical curves of the SRP branches. Among the branches only one of the SRP branches can be revealed

without these extra controllable parameters. In addition, the intersections of these critical curves correspond to the triple points of the system, where both the first- and the second-order phase transitions occur. Such a comparison between the QRR model and the QRS model in our work offers a way to seek exotic quantum phase transitions in matter-light coupled systems and provides an alternative method to investigate emergent phenomena induced by gauge phases in quantum materials.

Finally, we note that our QRS model can be regarded as a basic building block for a lattice system with periodic boundary conditions. The connection and difference between the artificial gauge phase and long-range hopping in a general lattice model is of particular interest in the exploration of exotic quantum phases and QPTs. For example, as demonstrated in Appendix C, our QRS model can be mapped to a frustrated J_1-J_2 spin model, which has been intensively investigated in quantum magnetism. Despite a few decades of active research [50–52], key questions such as the existence of a spin liquid phase remain unanswered. Further studies of the QRS model, especially in one-dimensional and two-dimensional lattices, may shed new light on the investigation of the J_1-J_2 spin model.

ACKNOWLEDGMENTS

This work was supported by Beijing Natural Science Foundation (Grant No. Z240007), the National Natural Science Foundation of China (Grants No. 12125402, No. 12074428, and No. 92265208), and the National Key R&D Program (Grant No. 2022YFA1405300). F.-X.S. acknowledges the China Postdoctoral Science Foundation for support (Grant No. 2020M680186). H.P. was supported by the U.S. NSF Grant No. PHY-2207283 and the Welch Foundation (Grant No. C-1669).

APPENDIX A: ORDER PARAMETERS FOR THE SRP

Notice that the first part of H in Eq. (7) is similar to Eq. (1), indicating that the Schrieffer-Wolff transformation can also be applied to project the Hamiltonian into the low-energy spin subspace $P_- \equiv |-\rangle\langle -|$. Typically, the local minimum can be determined by demanding $V = 0$. Considering the real and imaginary parts of V, the following equations can be derived from $\mathrm{Re}(V) = \mathrm{Im}(V) = 0$:

$$\begin{aligned}&\omega A_n - \lambda \sin(2\gamma_n) + J_1(A_{n+1} + A_{n-1}) + J_2 A_{n+2} = 0,\\ &\omega B_n + J_1(B_{n+1} + B_{n-1}) + J_2 B_{n+2} = 0.\end{aligned} \tag{A1}$$

Taking the periodic condition into consideration, we can easily get $B_1 + B_3 = B_2 + B_4 = 0$ and $B_n = 0$. Then the first of Eq. (A1) can be simplified as

$$\left(\omega - \frac{4\lambda^2}{\sqrt{16\lambda^2 A_n^2 + \Omega^2}}\right) A_n + J_1(A_{n-1} + A_{n+1}) + J_2 A_{n+2} = 0. \tag{A2}$$

One solution is obtained by assuming $A_1 = A_3 = a$ and $A_2 = A_4 = a'$, leading to

$$\begin{aligned}&\left(\omega + J_2 - \frac{4\lambda^2}{\sqrt{16\lambda^2 a^2 + \Omega^2}}\right) a + 2J_1 a' = 0,\\ &\left(\omega + J_2 - \frac{4\lambda^2}{\sqrt{16\lambda^2 a'^2 + \Omega^2}}\right) a' + 2J_1 a = 0.\end{aligned} \tag{A3}$$

Then we can obtain two solutions

$$\begin{aligned}a = a' &= \pm\frac{1}{4\lambda}\sqrt{\frac{16\lambda^4}{(\omega + J_2 + 2J_1)^2} - \Omega^2},\\ a = -a' &= \pm\frac{1}{4\lambda}\sqrt{\frac{16\lambda^4}{(\omega + J_2 - 2J_1)^2} - \Omega^2}.\end{aligned} \tag{A4}$$

The critical point is reached when $a^2 = a'^2 = 0$, giving $g_c = \frac{1}{2}\sqrt{1 + J_2/\omega + 2J_1/\omega}$ and $g_c = \frac{1}{2}\sqrt{1 + J_2/\omega - 2J_1/\omega}$, corresponding to the choice of $q = 0$ and π in Eq. (6), respectively. The twofold-degenerate ground states in both cases indicate the breaking of Z_2 symmetry.

Another case occurs when $A_1 = A_4 = a$ and $A_2 = A_3 = a'$. The conditions are

$$\begin{aligned}&\left(\omega - \frac{4\lambda^2}{\sqrt{16\lambda^2 a^2 + \Omega^2}}\right) a + J_1(a + a') + J_2 a' = 0,\\ &\left(\omega - \frac{4\lambda^2}{\sqrt{16\lambda^2 a'^2 + \Omega^2}}\right) a' + J_1(a + a') + J_2 a = 0.\end{aligned} \tag{A5}$$

If $a = a'$, the equations above will be reduced to the first case. The nontrivial solutions are

$$a = -a' = \pm\frac{1}{4\lambda}\sqrt{\frac{16\lambda^4}{(\omega - J_2)^2} - \Omega^2}. \tag{A6}$$

Thus, the critical point can be obtained as $g_c = \frac{1}{2}\sqrt{1 - J_2/\omega}$, which matches well with $g_c(q = \pi/2, 3\pi/2)$ in Eq. (6). Notice that the ground state breaks both the Z_2 and C_4 symmetries simultaneously, which means the fourfold-degenerate ground states occur if we consider the cyclic exchange of the four sites as $1234 \to 2341 \to 3412 \to 4123$.

APPENDIX B: ANALYSIS OF THE VALIDITY OF THE MEAN-FIELD SOLUTION

The analytical results presented in the main text are based on the mean-field approximation. Here we provide a quantitative comparison between the mean-field results and the fully numerical results based on the exact diagonalization of the original Hamiltonian (1). Specifically, we define the fidelity for our mean-field ground state as $f \equiv |\langle\psi_g|\psi_{\mathrm{num}}\rangle|^2$, where $|\psi_{\mathrm{num}}\rangle$ is the ground state from the full numerical calculation and

$$|\psi_g\rangle = D^\dagger(\vec{\alpha}) \prod_{2q/\pi=0}^{3} S_q(|0\rangle|-\rangle)^{\otimes 4} \tag{B1}$$

is the mean-field ground state. Note that in the NP, $\vec{\alpha} = \vec{0}$, $|-\rangle = |\downarrow\rangle$, and the squeezed operator S_q is defined in

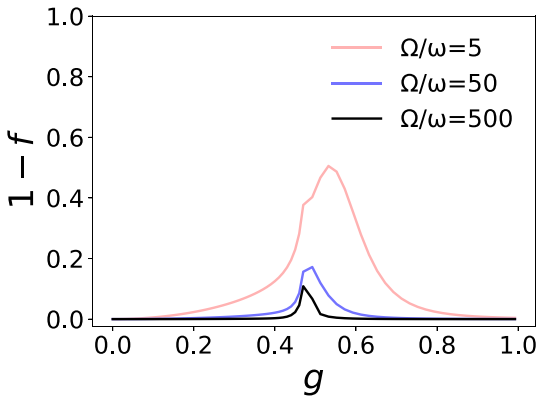

FIG. 5. Infidelity between the mean-field ground state ψ_g and the numerical ground state ψ_{num} with fixed hopping rates $J_1 = 0.05$ and $J_2 = 0.07$ in our QRS model.

Sec. III, while in the SRP, the squeezed parameter is changed as $\lambda_q[g] \to \lambda_q[g' = g_c^3(q)/g^2]$.

We illustrate in Fig. 5 the infidelity $1 - f$ as a function of the coupling strength g. We find that the infidelity is always small (i.e., $1 - f \sim 0$) far away from the critical point. By contrast, near the critical point, the infidelity increases sharply. However, this error can be greatly suppressed by increasing the ratio Ω/ω, suggesting that the mean field becomes essentially exact in the thermodynamic limit $\Omega/\omega \to \infty$. We want to point out that the exact diagonalization near the critical point poses a challenging numerical problem, due to the divergent photon number. Here we set a cutoff of the bosonic mode dimension as $N_c = 5$ to guarantee convergence not too close to the critical point, which is sufficient to provide qualitative conclusions.

APPENDIX C: MAPPING TO THE SPIN J_1-J_2 MODEL

By means of the Holstein-Primakoff transformation, given by $S_n^z = a_n^\dagger a_n - S_n$ and $S_n^+ = a_n^\dagger \sqrt{2S_n - a_n^\dagger a_n} \approx a_n^\dagger \sqrt{2S_n}$, where the classic spin limit $S_n = S \to \infty$ is applied, the Hamiltonian (3) can be mapped into a four-lattice J_1-J_2 model as

$$H_{J_1J_2} = \sum_{n=1}^{4} \left(\omega S_n^z - \frac{2g^2\omega}{S}\left(S_n^x\right)^2\right) + \frac{J_1}{S}\sum_{n=1}^{4}\left(S_n^x S_{n+1}^x + S_n^y S_{n+1}^y\right) + \frac{J_2}{2S}\sum_{n=1}^{4}\left(S_n^x S_{n+2}^x + S_n^y S_{n+2}^y\right). \tag{C1}$$

By defining $X_n \equiv \langle S_n^x\rangle/S$ and $Y_n \equiv \langle S_n^y\rangle/S$, the mean-field energy of such a spin Hamiltonian is expressed as

$$\frac{E_{J_1J_2}}{\omega S} = \sum_{n=1}^{4}\left(-\sqrt{1 - X_n^2 - Y_n^2} - 2g^2X_n^2 + J_1(X_nX_{n+1} + Y_nY_{n+1}) + \frac{J_2}{2}(X_nX_{n+2} + Y_nY_{n+2})\right). \tag{C2}$$

A minimization of the energy $E_{J_1J_2}$ can give similar branches of solutions for $\{\langle\vec{S}_n\rangle\}$, i.e.,

$$X_n = X_{n+1} = X_{n+2} = \pm\sqrt{1 - \left(\frac{1}{4g^2 - 4[g_c(0)]^2 + 1}\right)^2}, \tag{C3}$$

$$X_n = X_{n+2} = -X_{n+1} = \pm\sqrt{1 - \left(\frac{1}{4g^2 - 4[g_c(\pi)]^2 + 1}\right)^2}, \tag{C4}$$

and

$$X_n = X_{n+1} = -X_{n+2} = \pm\sqrt{1 - \left(\frac{1}{4g^2 - 4[g_c(\pi/2)]^2 + 1}\right)^2}, \tag{C5}$$

with the spin-y components $Y_n = 0$ in all three cases. Obviously, the arrangements for spin-x components X_n correspond to the optical displacement A_n in all three different superradiant branches, shown as Eqs. (A4) and (A6). In addition, the dimensionless coupling strengths g will be reduced to the critical points g_c when $X_n = 0$.

[1] K. Hepp and E. H. Lieb, On the superradiant phase transition for molecules in a quantized radiation field: The Dicke maser model, Ann. Phys. (NY) **76**, 360 (1973).

[2] Y. K. Wang and F. T. Hioe, Phase transition in the Dicke model of superradiance, Phys. Rev. A **7**, 831 (1973).

[3] C. Emary and T. Brandes, Quantum chaos triggered by precursors of a quantum phase transition: The Dicke model, Phys. Rev. Lett. **90**, 044101 (2003).

[4] C. Emary and T. Brandes, Chaos and the quantum phase transition in the Dicke model, Phys. Rev. E **67**, 066203 (2003).

[5] M.-J. Hwang, R. Puebla, and M. B. Plenio, Quantum phase transition and universal dynamics in the Rabi model, Phys. Rev. Lett. **115**, 180404 (2015).

[6] M.-J. Hwang and M. B. Plenio, Quantum phase transition in the finite Jaynes-Cummings lattice systems, Phys. Rev. Lett. **117**, 123602 (2016).

[7] F. Dimer, B. Estienne, A. S. Parkins, and H. J. Carmichael, Proposed realization of the Dicke-model quantum phase transition in an optical cavity QED system, Phys. Rev. A **75**, 013804 (2007).

[8] A. Bermudez and M. B. Plenio, Spin Peierls quantum phase transitions in Coulomb crystals, Phys. Rev. Lett. **109**, 010501 (2012).

[9] K. Baumann, C. Guerlin, F. Brennecke, and T. Esslinger, Dicke quantum phase transition with a superfluid gas in an optical cavity, Nature (London) **464**, 1301 (2010).

[10] I. Bloch, J. Dalibard, and S. Nascimbène, Quantum simulations with ultracold quantum gases, Nat. Phys. **8**, 267 (2012).

[11] M. L. Cai, Z. D. Liu, W. D. Zhao, Y. K. Wu, Q. X. Mei, Y. Jiang, L. He, X. Zhang, Z. C. Zhou, and L. M. Duan, Observation of a quantum phase transition in the quantum Rabi model with a single trapped ion, Nat. Commun. **12**, 1126 (2021).

[12] S. Ebadi, T. T. Wang, H. Levine, A. Keesling, G. Semeghini, A. Omran, D. Bluvstein, R. Samajdar, H. Pichler, W. W. Ho, S. Choi, S. Sachdev, M. Greiner, V. Vuletić, and M. D. Lukin, Quantum phases of matter on a 256-atom programmable quantum simulator, Nature (London) **595**, 227 (2021).

[13] N. K. Langford, R. Sagastizabal, M. Kounalakis, C. Dickel, A. Bruno, F. Luthi, D. J. Thoen, A. Endo, and L. DiCarlo, Experimentally simulating the dynamics of quantum light and matter at deep-strong coupling, Nat. Commun. **8**, 1715 (2017).

[14] P. Forn-Díaz, J. Lisenfeld, D. Marcos, J. J. García-Ripoll, E. Solano, C. J. P. M. Harmans, and J. E. Mooij, Observation of the Bloch-Siegert shift in a qubit-oscillator system in the ultrastrong coupling regime, Phys. Rev. Lett. **105**, 237001 (2010).

[15] Y. Todorov, A. M. Andrews, I. Sagnes, R. Colombelli, P. Klang, G. Strasser, and C. Sirtori, Strong light-matter coupling in subwavelength metal-dielectric microcavities at terahertz frequencies, Phys. Rev. Lett. **102**, 186402 (2009).

[16] F. Yoshihara, T. Fuse, S. Ashhab, K. Kakuyanagi, S. Saito, and K. Semba, Superconducting qubit–oscillator circuit beyond the ultrastrong-coupling regime, Nat. Phys. **13**, 44 (2017).

[17] P. Forn-Díaz, J. J García-Ripoll, B. Peropadre, J. L. Orgiazzi, M. A Yurtalan, R. Belyansky, C. M Wilson, and A. Lupascu, Ultrastrong coupling of a single artificial atom to an electromagnetic continuum in the nonperturbative regime, Nat. Phys. **13**, 39 (2017).

[18] H. J. Kimble, The quantum internet, Nature (London) **453**, 1023 (2008).

[19] Q.-X. Mei, B.-W. Li, Y.-K. Wu, M.-L. Cai, Y. Wang, L. Yao, Z.-C. Zhou, and L.-M. Duan, Experimental realization of the Rabi-Hubbard model with trapped ions, Phys. Rev. Lett. **128**, 160504 (2022).

[20] Y.-Y. Zhang, Z.-X. Hu, L. Fu, H.-G. Luo, H. Pu, and X.-F. Zhang, Quantum phases in a quantum Rabi triangle, Phys. Rev. Lett. **127**, 063602 (2021).

[21] D. F. Padilla, H. Pu, G.-J. Cheng, and Y.-Y. Zhang, Understanding the quantum Rabi ring using analogies to quantum magnetism, Phys. Rev. Lett. **129**, 183602 (2022).

[22] R. Grimaudo, A. S. M. de Castro, A. Messina, E. Solano, and D. Valenti, Quantum phase transitions for an integrable quantum Rabi-like model with two interacting qubits, Phys. Rev. Lett. **130**, 043602 (2023).

[23] Y. Wang, M. Liu, W.-L. You, S. Chesi, H.-G. Luo, and H.-Q. Lin, Resilience of the superradiant phase against $\mathbf{A}^2$ effects in the quantum Rabi dimer, Phys. Rev. A **101**, 063843 (2020).

[24] L.-J. Li, L.-L. Feng, J.-H. Dai, and Y.-Y. Zhang, Quantum Rabi hexagonal ring in an artificial magnetic field, Phys. Rev. A **108**, 043705 (2023).

[25] S. Ashhab, Superradiance transition in a system with a single qubit and a single oscillator, Phys. Rev. A **87**, 013826 (2013).

[26] M. Schiró, M. Bordyuh, B. Öztop, and H. E. Türeci, Phase transition of light in cavity QED lattices, Phys. Rev. Lett. **109**, 053601 (2012).

[27] C. J. Zhu, L. L. Ping, Y. P. Yang, and G. S. Agarwal, Squeezed light induced symmetry breaking superradiant phase transition, Phys. Rev. Lett. **124**, 073602 (2020).

[28] M. Soriente, T. Donner, R. Chitra, and O. Zilberberg, Dissipation-induced anomalous multicritical phenomena, Phys. Rev. Lett. **120**, 183603 (2018).

[29] L. Bakemeier, A. Alvermann, and H. Fehske, Quantum phase transition in the Dicke model with critical and noncritical entanglement, Phys. Rev. A **85**, 043821 (2012).

[30] X.-Y. Lü, L.-L. Zheng, G.-L. Zhu, and Y. Wu, Single-photon-triggered quantum phase transition, Phys. Rev. Appl. **9**, 064006 (2018).

[31] J. Zhao and M.-J. Hwang, Frustrated superradiant phase transition, Phys. Rev. Lett. **128**, 163601 (2022).

[32] A. Baksic and C. Ciuti, Controlling discrete and continuous symmetries in superradiant phase transitions with circuit QED systems, Phys. Rev. Lett. **112**, 173601 (2014).

[33] R. Puebla, M.-J. Hwang, J. Casanova, and M. B. Plenio, Probing the dynamics of a superradiant quantum phase transition with a single trapped ion, Phys. Rev. Lett. **118**, 073001 (2017).

[34] J. Zhao and M.-J. Hwang, Anomalous criticality with bounded fluctuations and long-range frustration induced by broken time-reversal symmetry, Phys. Rev. Res. **5**, L042016 (2023).

[35] L. Duan, Y.-Z. Wang, and Q.-H. Chen, Quantum phase transitions in the triangular coupled-top model, Phys. Rev. B **107**, 094415 (2023).

[36] G. Hu, Z. Lü, H. Lin, and H. Zheng, Hopping-induced quantum phase transition in the Ising-Rabi lattice model, Phys. Rev. A **108**, 023723 (2023).

[37] J.-M. Cheng, Y.-C. Zhang, X.-F. Zhou, and Z.-W. Zhou, Quantum phase transitions in the anti-Jaynes-Cummings triangle model, New J. Phys. **25**, 103048 (2023).

[38] L. S. Madsen, F. Laudenbach, M. F. Askarani, F. Rortais, T. Vincent, J. F. F. Bulmer, F. M. Miatto, L. Neuhaus, L. G. Helt, M. J. Collins, A. E. Lita, T. Gerrits, S. W. Nam, V. D. Vaidya, M. Menotti, I. Dhand, Z. Vernon, N. Quesada, and J. Lavoie, Quantum computational advantage with a programmable photonic processor, Nature (London) **606**, 75 (2022).

[39] M. Li, D. Zhirihin, M. Gorlach, X. Ni, D. Filonov, A. Slobozhanyuk, A. Alù, and A. B. Khanikaev, Higher-order topological states in photonic kagome crystals with long-range interactions, Nat. Photon. **14**, 89 (2020).

[40] M. Tian, F. Sun, K. Shi, H. Xu, Q. He, and W. Zhang, Nonreciprocal amplification transition in a topological photonic network, Photon. Res. **11**, 852 (2023).

[41] H. Li, Z. Dong, S. Longhi, Q. Liang, D. Xie, and B. Yan, Aharonov-Bohm caging and inverse Anderson transition in ultracold atoms, Phys. Rev. Lett. **129**, 220403 (2022).

[42] C. Zeng, Y.-R. Shi, Y.-Y. Mao, F.-F. Wu, Y.-J. Xie, T. Yuan, W. Zhang, H.-N. Dai, Y.-A. Chen, and J.-W. Pan, Transition from flat-band localization to Anderson localization in a one-dimensional Tasaki lattice, Phys. Rev. Lett. **132**, 063401 (2024).

[43] C. Monroe, W. C. Campbell, L.-M. Duan, Z.-X. Gong, A. V. Gorshkov, P. W. Hess, R. Islam, K. Kim, N. M. Linke, G. Pagano, P. Richerme, C. Senko, and N. Y. Yao, Programmable quantum simulations of spin systems with trapped ions, Rev. Mod. Phys. **93**, 025001 (2021).

[44] A. A. Houck, H. E. Türeci, and J. Koch, On-chip quantum simulation with superconducting circuits, Nat. Phys. **8**, 292 (2012).

[45] S. Sachdev and R. N. Bhatt, Bond-operator representation of quantum spins: Mean-field theory of frustrated quantum Heisenberg antiferromagnets, Phys. Rev. B **41**, 9323 (1990).

[46] A. V. Chubukov and T. Jolicoeur, Dimer stability region in a frustrated quantum Heisenberg antiferromagnet, Phys. Rev. B **44**, 12050 (1991).

[47] M. E. Zhitomirsky and K. Ueda, Valence-bond crystal phase of a frustrated spin-1/2 square-lattice antiferromagnet, Phys. Rev. B **54**, 9007 (1996).

[48] R. O. Umucalılar and I. Carusotto, Artificial gauge field for photons in coupled cavity arrays, Phys. Rev. A **84**, 043804 (2011).

[49] D. L. Underwood, W. E. Shanks, J. Koch, and A. A. Houck, Low-disorder microwave cavity lattices for quantum simulation with photons, Phys. Rev. A **86**, 023837 (2012).

[50] J. Sirker, Z. Weihong, O. P. Sushkov, and J. Oitmaa, J_1-J_2 model: First-order phase transition versus deconfinement of spinons, Phys. Rev. B **73**, 184420 (2006).

[51] S.-S. Gong, D. N. Sheng, O. I. Motrunich, and M. P. A. Fisher, Phase diagram of the spin-$\frac{1}{2}$ J_1-J_2 Heisenberg model on a honeycomb lattice, Phys. Rev. B **88**, 165138 (2013).

[52] O. Gauthé and F. Mila, Thermal Ising transition in the spin-$1/2$ J_1-J_2 Heisenberg model, Phys. Rev. Lett. **128**, 227202 (2022).